Chipscale plasmonic modulators and switches based on metal–insulator–metal waveguides with Ge$_2$Sb$_2$Te$_5$

Zhaojian Zhang
Junbo Yang
Wei Bai
Yunxin Han
Xin He
Jingjing Zhang
Jie Huang
Dingbo Chen
Siyu Xu
Wanlin Xie

SPIE.

Chipscale plasmonic modulators and switches based on metal–insulator–metal waveguides with Ge$_2$Sb$_2$Te$_5$

Zhaojian Zhang,^{a} Junbo Yang,^{b,}* Wei Bai,^{c} Yunxin Han,^{b} Xin He,^{b} Jingjing Zhang,^{a} Jie Huang,^{a} Dingbo Chen,^{a} Siyu Xu,^{a} and Wanlin Xie^a

^{a}National University of Defense Technology, College of Liberal Arts and Sciences, Changsha, China
^{b}National University of Defense Technology, Center of Material Science, Changsha, China
^{c}Chinese Academy of Sciences, Institute of Optics and Electronics, Chengdu, China

Abstract. We introduce phase-change material Ge$_2$Sb$_2$Te$_5$ (GST) into metal–insulator–metal (MIM) waveguide systems to realize chipscale plasmonic modulators and switches in the telecommunication band. Benefitting from the high contrast of optical properties between amorphous and crystalline GST, the three proposed structures can act as reconfigurable and nonvolatile modulators and switches with excellent modulation depth 14 dB and fast response time in subnanosecond while possessing small footprints, simple frameworks, and easy fabrication. We provide solutions to design active devices in MIM waveguide systems and can find potential applications in more compact all-optical circuits for information processing and storage. © 2019 Society of Photo-Optical Instrumentation Engineers (SPIE) [DOI: 10.1117/1.JNP.13.046009]

1 Introduction

Facing the increasing demand for information quantity and transmission rate, today's electronic integrated devices will be unable to afford roles in future chipscale systems due to the fundamental limits.[1] As a promising solution, photonic integrated devices can break the blocks by using light as the carrier of information. To construct basic photonic circuits, dielectric waveguides (such as silicon waveguide) have been widely studied for decades.[2,3] However, the scale of a dielectric waveguide cannot go smaller than the working wavelength due to the diffraction limit, which restricts the integration and compactness of photonic integrated chips.[1] Recently, surface plasmon polariton (SPPs), which are the surface electromagnetic waves supported at the interface between metal and dielectric, have attracted more attention due to the capacity to break the diffraction limit.[1] SPPs also introduce plasmonic waveguides, which can deliver light in subwavelength scale.[4,5] In particular, plasmonic metal–insulator–metal (MIM) waveguides possess good confinement of light, low bending loss, easy fabrication, and acceptable propagation length and, therefore, can be potential platforms for more compact all-optical integrated circuits.[6–9]

As the promising next-generation on-chip photonic system, MIM system has supported various chipscale passive devices, such as filters,[10,11] demultiplexers,[12,13] sensors,[14,15] and spacers.[16,17] However, active devices are also required in such a system. Therefore, optical materials with tunable properties have been utilized to realize dynamically tunable functionalities. For example, nonlinear materials have been used to realize all-optical tunable filters, logic gates, and diodes.[18–20] Lasers, switches, and slow light enhancement can be achieved by integrating gain materials.[21–23] Two-dimension (2-D) materials have contributed to the active manipulation of MIM waveguides as well.[24–26] Some optical concepts, such as epsilon-near-zero effects and

---

non-PT-symmetry, have also been made possible in MIM systems assisted by optical materials.[27,28] Obviously, optical materials will play an important role in active systems, and it is essential to explore more outcomes from the combination between MIM waveguides and optical materials. Recently, phase-change materials, such as $Ge_2Sb_2Te_5$ (GST), have drawn more attention. GST possesses tremendously different optical properties from amorphous to crystalline states. Such a phase transition can be triggered by thermal, electrical, or optical schemes, has an ultrafast switching time in nanosecond (ns) or even sub-ns, and is usually reversible.[29] Until now, GST has been regarded as a strong candidate for realizing reconfigurable and nonvolatile all-optical devices for data processing and storage,[30] and many applications have been proposed such as on-chip memory elements,[31–33] all-optical switching,[34–36] and reconfigurable metasurfaces.[37–39]

Here, we introduce GST into MIM systems to realize chipscale plasmonic modulators and switches in shortwave infrared (SWIR) telecommunication regime. Combining metal–silicon–metal (MSM) waveguides and metal–GST–metal (MGM) resonators, we numerically propose three typical MIM structures, including end-coupled rectangular resonator, side-coupled stub resonator, and two mutually coupled resonators, to investigate their performances on transmission modulations. Due to the phase transition of GST, the effective refractive index inside MGM resonators can be actively tuned with high contrast, consequently leading to the significant shifts of resonant wavelengths. Benefitting from this, the three proposed structures can act as reconfigurable and nonvolatile modulators and switches with excellent modulation depth (MD) and fast response time, meanwhile possessing small footprints. Besides, compared with resonators with other shapes (ring, disk, etc.) in MIM systems, the stub resonator in this work has a simpler framework and can be fabricated easily.[18–20] This work provides new solutions to design active devices based on MIM systems and can find potential applications in future on-chip all-optical circuits.

2 Structures, Materials, and Methods

The first proposed structure is shown in Fig. 1, consisting of input and output MSM waveguides end-coupled with an MGM rectangular resonator. The geometric parameters are as follows: the width of waveguide $w = 50$ nm, the gap $g = 20$ nm, and the length of resonator $L = 120$ nm.

In Fig. 1, the gray area is silver (Ag), the dielectric constant of which is defined by the Drude model[10]

$$\varepsilon_m = \varepsilon_\infty - \frac{\omega_p^2}{\omega(\omega + i\gamma)}, \tag{1}$$

where ε_m is the dielectric constant of Ag, ε_∞ is the dielectric constant at infinite frequency, ω_p is the bulk plasma frequency, γ is the electron oscillation damping frequency, and ω is the angular frequencies of incident waves. The parameters of Ag are as follows: $\varepsilon_\infty = 3.7$, $\omega_p = 1.38 \times 10^{16}$ Hz, and $\gamma = 2.73 \times 10^{13}$ Hz. The waveguides are filled with silicon (Si) due
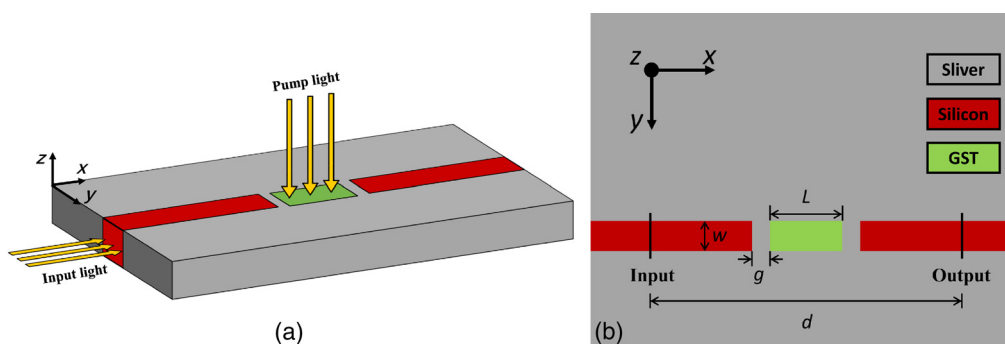

Fig. 1 (a) The 3-D schematic of the first structure. (b) The top view of the first structure.
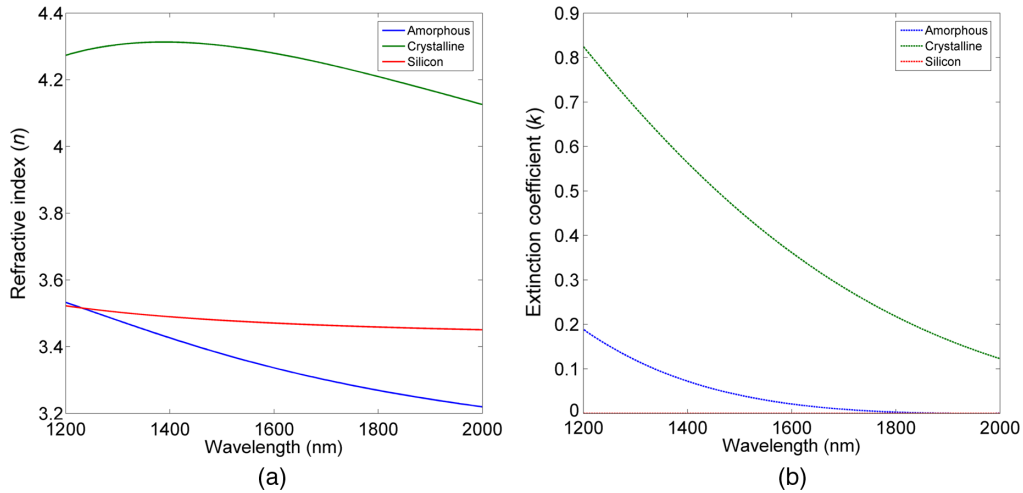
Fig. 2 (a) The refractive index of amorphous GST, crystalline GST, and silicon. (b) The extinction coefficient of amorphous GST, crystalline GST, and silicon.

to the low dispersion and loss in SWIR, which is shown in red in Fig. 1, and the corresponding optical constant $(n + ik)$ is shown in Fig. 2.[40] GST possesses dramatically different optical properties between the amorphous (aGST) and crystalline state (cGST), and the corresponding optical constants are also shown in Fig. 2.[41] We can see that there is a high contrast in refractive index between the two states, and cGST possesses much more intrinsic loss than aGST in SWIR. The effective dielectric constants of GST with different crystallinities are predicted by the Lorentz–Lorenz relation[42]

$$\frac{\varepsilon_{\mathrm{GST}}(\lambda, C) - 1}{\varepsilon_{\mathrm{GST}}(\lambda, C) - 1} = C \times \frac{\varepsilon_{\mathrm{cGST}}(\lambda) - 1}{\varepsilon_{\mathrm{cGST}}(\lambda) + 2} + (1 - C) \times \frac{\varepsilon_{\mathrm{aGST}}(\lambda) - 1}{\varepsilon_{\mathrm{aGST}}(\lambda) + 2}. \tag{2}$$

Here, $\varepsilon_{\mathrm{aGST}}$ and $\varepsilon_{\mathrm{cGST}}$ are dielectric constants of aGST and cGST, respectively. C is the crystallization fraction of GST from 0 to 1. The crystallinity can be tuned by the pump light as shown in Fig. 1(a).

In the MIM waveguide, only the fundamental transverse-magnetic (TM) mode propagates. The dispersion of fundamental mode is described as follows:[6]

$$\frac{\varepsilon_i \sqrt{\beta^2 - \varepsilon_m k_0^2}}{\varepsilon_m \sqrt{\beta^2 - \varepsilon_i k_0^2}} + \tanh\left(\frac{w\sqrt{\beta^2 - \varepsilon_i k_0^2}}{2}\right) = 0, \tag{3}$$

where ε_i is the dielectric constant of the insulator (Si or GST), $k_0 = 2\pi/\lambda_0$ represents the wavevector in free space, and β is the wavevector of SPPs inside the MIM waveguide. The effective refractive index is defined as $n_{\mathrm{eff}} = \beta/k_0$. The calculated n_{eff} of fundamental TM mode in the MSM waveguide as well as the MGM waveguide in different crystallization conditions are shown in Figs. 3(a) and 3(b). The profile of fundamental TM mode in the MSM waveguide is shown in Fig. 3(c), and the mode in the MGM waveguide has the similar profile. Two-dimensional (2-D) finite-difference time-domain method is applied to do the simulation, which is mostly used in previous works.[10–17] It has been reported that 2-D model has the same simulated results as three-dimensional (3-D) model when the height (the length in the z-direction) of the metal is sufficiently high.[43] The mesh size is set as 3 nm to ensure the accuracy, and the boundary condition is set as perfectly matched layers to maintain convergence. Two power monitors are placed at input and output, respectively, and the distance between the two monitors is $d = 500$ nm. The transmission is calculated following $T = P_{\mathrm{out}}/P_{\mathrm{in}}$.
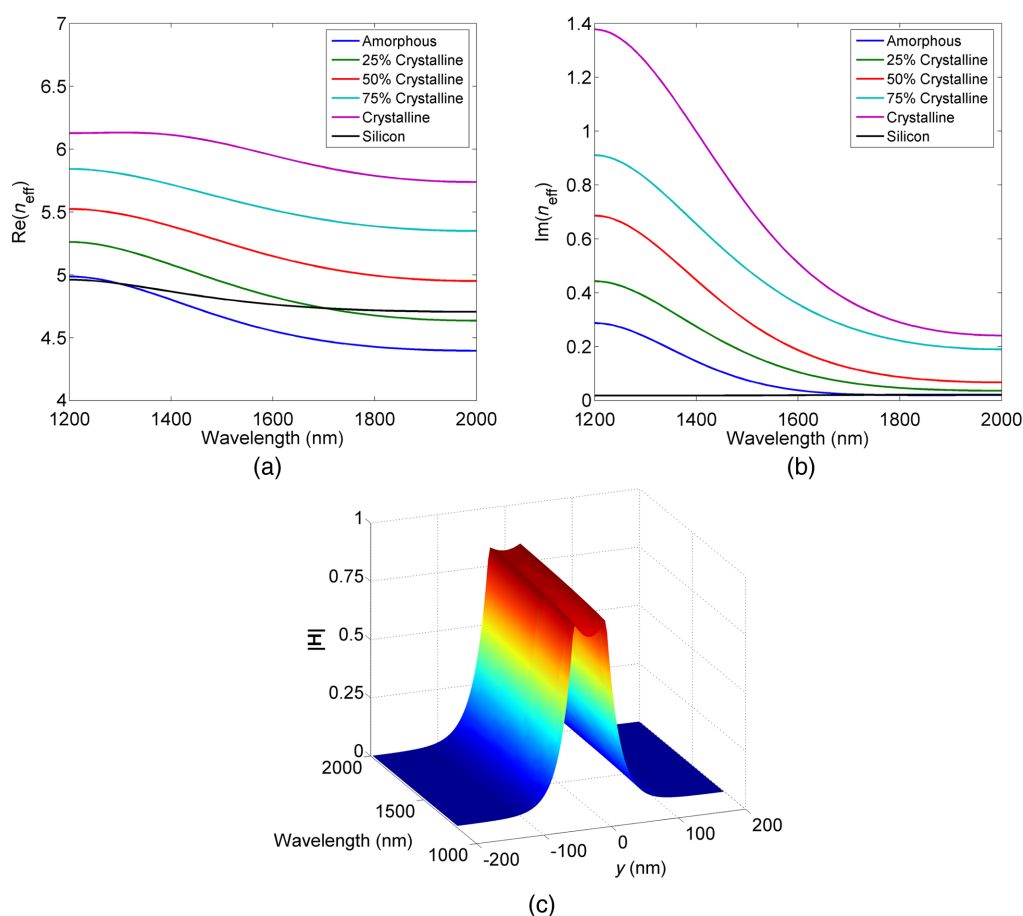
Fig. 3 (a) The real part of effective refractive index. (b) The imaginary part of effective refractive index. (c) The profile of fundamental TM mode in the MSM waveguide.

3 Results and Discussions

The transmission spectrum of the structure in Fig. 1 corresponding to different phase states of GST is shown in Fig. 4(a). In MIM system, such structure is a typical band-pass filter. The rectangular resonator acts as a Fabry–Perot (F-P) resonator, only the resonant wavelength can be coupled into this resonator from the input waveguide and released to the output waveguide. The resonant condition is as follows:[44]

$$\left(2m - \frac{\varphi}{\pi}\right)\lambda = 4\,\mathrm{Re}(n_{\mathrm{eff}})L, \quad m = 1,2\ldots, \tag{4}$$

where m is the mode number, which is an integer. φ is the phase shift induced by the reflection at the insulator–metal interface. As shown in Fig. 4(a) in blue, the passed resonant wavelength is 1527 nm when GST is in amorphous state, the transmission of which is 44%. The corresponding magnitude of magnetic field $|\mathbf{H}|$ distribution is shown in Fig. 4(b), from which we can see that there exists an F-P mode with $m = 1$ in the rectangular resonator, and SPPs can pass through such structure. However, when GST comes to crystalline state, the transmission peak will have a redshift due to the increase of $\mathrm{Re}(n_{\mathrm{eff}})$ as shown in Fig. 4(a). Meanwhile, the amplitude of the peak will decline, caused by the rise of material loss. Benefitting from this, the transmission at 1527 nm can be actively tuned from 44% to 1.8%, the corresponding $|\mathbf{H}|$ distribution is shown in Fig. 4(c), showing that transmitted SPPs are suppressed. To evaluate the performance of transmission modulation, the MD is defined as follows:
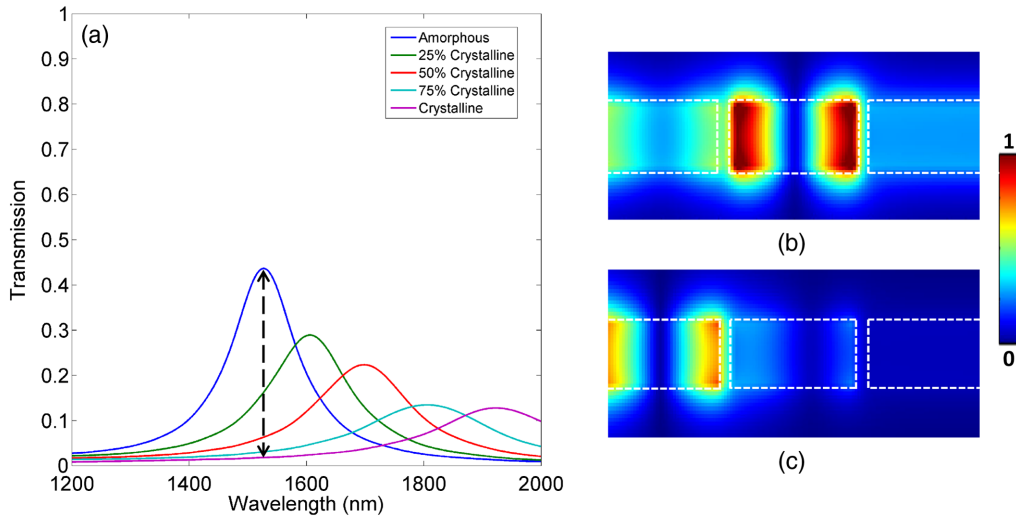
Fig. 4 (a) The transmission spectrum corresponding to different phase states of GST. (b) The |**H**| distribution at 1527 nm in GST amorphous state. (c) The |**H**| distribution at 1527 nm in GST crystalline state.

$$\mathrm{MD} = \frac{T_{\max} - T_{\min}}{T_{\max}} \times 100\%, \tag{5}$$

where $T_{\max}$ and $T_{\min}$ are maximum and minimum transmission values, respectively. For convenience, we also provide modulation results in log scale:

$$\mathrm{IL}\,(\text{Insertion loss}) = -10\,\lg(T) \quad \mathrm{MD}_{\mathrm{dB}} = -10\,\lg(T_{\min}/T_{\max}). \tag{6}$$

The corresponding modulation results are shown in Table 1. From the aGST to cGST, the MD can reach 96% (13.8 dB).

Next, we introduce the second structure, a main MSM waveguide side-coupled with an MGM stub resonator, as shown in Fig. 5. The geometric parameters are as follows: $w = 50$ nm and $L = 200$ nm. The other parameters are unchanged.

Such structure is a typical band-stop filter in MIM system. The stub resonator can be seen as a semi F-P resonator, can trap the resonant wavelength, and prevent it from passing; the resonant condition is as follows:[45]

$$\left(2n + 1 - \frac{\varphi}{\pi}\right)\lambda = 4\,\mathrm{Re}(n_{\mathrm{eff}})L, \quad n = 0,1\ldots, \tag{7}$$

where n is the mode number. The transmission spectrum corresponding to different phase states of GST are shown in Fig. 6(a). Due to the high contrast between the refractive index of aGST and cGST, a giant redshift of transmission dip happens. Consequently, the transmission at 1513 nm can be modulated from 2.1% (16.8 dB) to 57% (2.4 dB), leading to an excellent MD 96% (14.4 dB), the details are given in Table 2. The |**H**| distribution at 1513 nm corresponding to aGST and cGST is shown in Figs. 6(b) and 6(c), respectively, indicating $n = 1$.

Table 1 The transmission as well as insertion loss in different GST states and the MD.

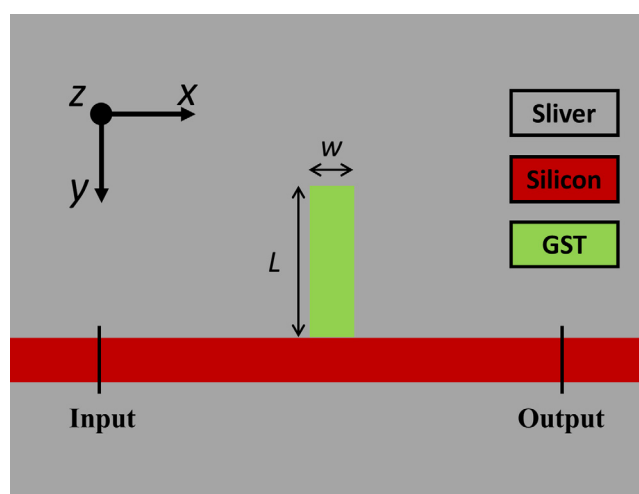| GST state	a	25% c	50% c	75% c	c	MD
T	44%	16%	6.3%	3.1%	1.8%	96%
IL	3.6 dB	8.0 dB	12.0 dB	15.1 dB	17.4 dB	13.8 dB

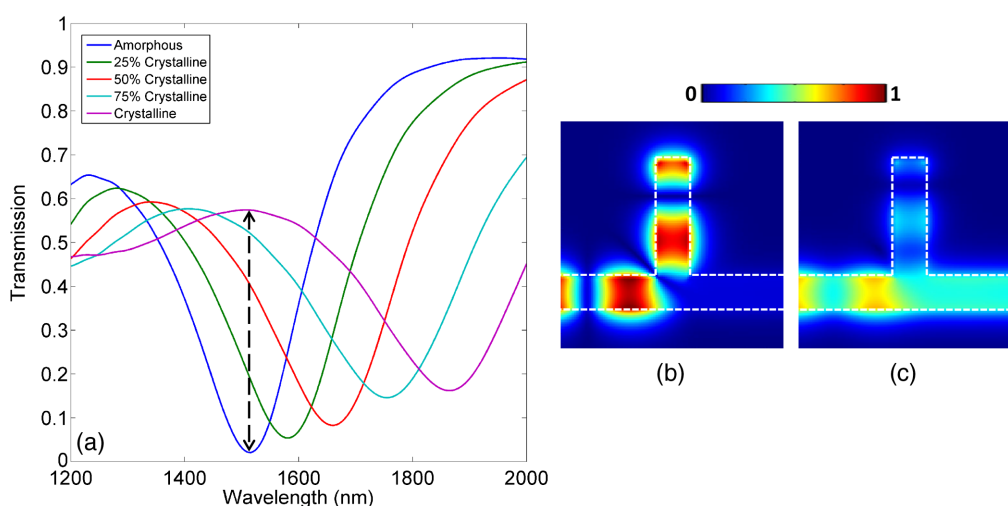**Fig. 5** The schematic of the second structure.

Fig. 6 (a) The transmission spectrum corresponding to different phase states of GST. (b) The |**H**| distribution at 1513 nm in GST amorphous state. (c) The |**H**| distribution at 1513 nm in GST crystalline state.

Table 2 The transmission as well as insertion loss in different GST states and the MD.

GST state	a	25% c	50% c	75% c	c	MD
T	2.1%	19%	41%	52%	57%	96%
IL	16.8 dB	7.2 dB	3.9 dB	2.8 dB	2.4 dB	14.4 dB

The last structure is shown in Fig. 7, including a main MSM waveguide side-coupled with a stub resonator and a rectangular resonator. The geometric parameters are as follows: $h = 45$ nm, $g = 15$ nm, $L = 110$ nm, and $w = 50$ nm. The other parameters are unchanged.

Such structure can produce plasmon-induced transparency (PIT) effect, which is a special case of Fano resonance. When this is the only stub resonator, a transmission dip exists as shown in Fig. 8(a) in blue. However, when the rectangular resonator is coupled upside the stub resonator, a transmission peak will appear at the position of the original dip as given in Fig. 8(a) in green, which is called PIT. Such effect attributes to the near-field interaction between
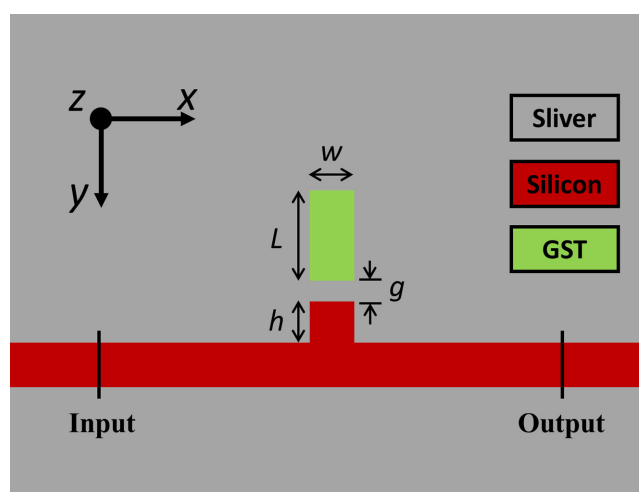
Fig. 7 The schematic of the third structure.

the mode in the stub (radiative mode) and the mode in the rectangle (subradiant mode). When the two modes have close resonant wavelengths, constructive interference will happen between the two modes, consequently leading to that transparent window.[46]

Here, we utilize GST to tune the resonant wavelengths of the subradiant mode and further control the interference to realize switching. When GST is amorphous, the resonant wavelengths of radiative and subradiant modes are close to each other, therefore leading to an induced transparent peak at 1479 nm as shown in Fig. 8(b) in blue. However, when it comes to cGST, the resonant wavelength of subradiant mode is shifted away, leading to no interference, i.e., a transmission dip at 1479 nm as shown in Fig. 8(b) in green. The corresponding $|\mathbf{H}|$ distributions are
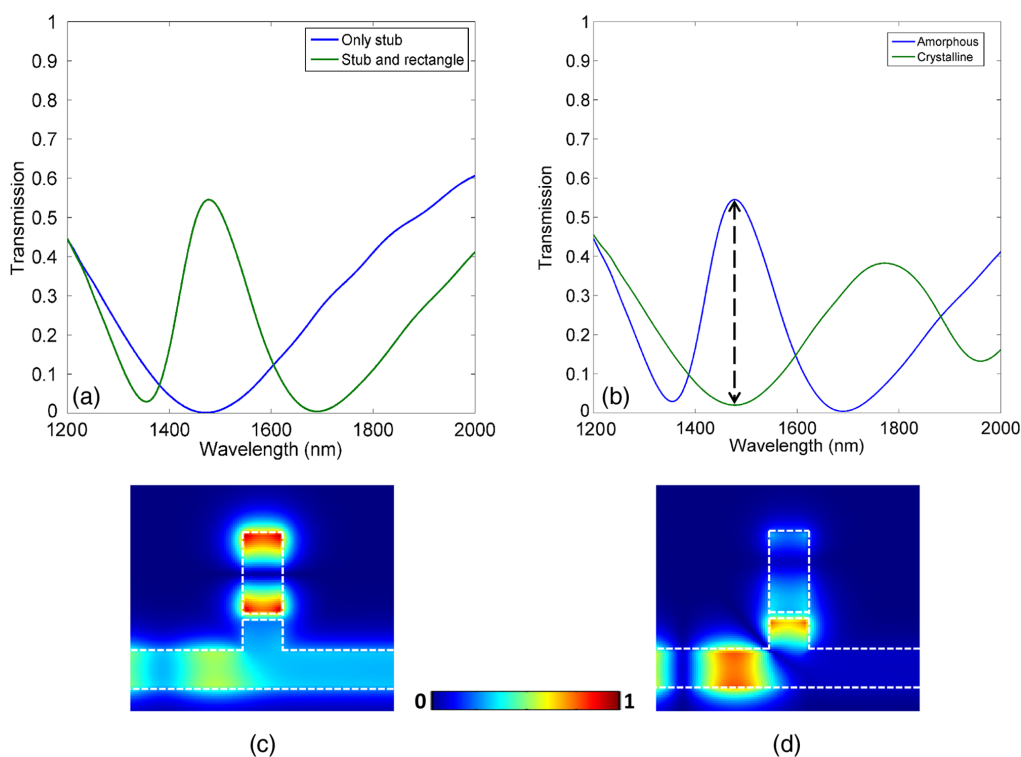

Fig. 8 (a) The transmission spectrum corresponding to the only stub as well as stub plus rectangle. (b) The transmission spectrum corresponding to aGST and cGST. (c) The $|\mathbf{H}|$ distribution at 1479 nm in aGST. (d) The $|\mathbf{H}|$ distribution at 1479 nm in cGST.

Table 3 The performance comparison between various MIM-based plasmonic modulators.

References	47	48	49	50	51	This work
MD	3 dB (50%)	4 dB (60%)	14 dB	12 dB	92%	13.8 and 14.4 dB (96%)
Embedded active material	Electro-optic crystal	Quantum dots-doped material	Nonlinear Kerr material	Electro-optic polymer	Magneto-optical material	GST
Response time	~100 fs	~40 ns	~200 fs	~100 fs	~1 ns	~500 ps

given in Figs. 8(c) and 8(d), respectively. The transmission at 1479 nm can be switched from 55% (2.6 dB) to 2% (17.0 dB), the MD can be up to 96% (14.4 dB), which is promising for all-optical switching.

Finally, we compare this work with other MIM plasmonic modulators.[47–51] It has to be mentioned that those MIM modulators also have similar scales with this work, several hundred nanometers in device length. Therefore, the MD of those modulators are directly provided for comparison in Table 3. Obviously, due to the high contrast of optical properties between the two states of GST, the GST-embedded modulators can have a better performance in MD. Another two important factors for modulators are the operation speed, which mainly dependent on the response time of the embedded materials, as well as the energy consumption. Table 3 shows that quantum dots-doped material and magneto-optical material only have response time in ns.[48,52] Electro-optic materials as well as Kerr material possess ultrafast response time in hundreds of femtoseconds (fs),[47,53] whereas GST can have response time in sub-ns.[54] However, electro-optic modulators cannot fulfill all-optical modulation, and Kerr material always requires ultrahigh pump intensity up to GW/cm^2 due to the small third-order nonlinear susceptibility.[55] Nevertheless, it has been reported that turning aGST to cGST only requires a low energy consumption, a small voltage 1 V or pump intensity 9.5 W/cm^2.[54,56] Therefore, considering the three factors above, GST-embedded modulator can be a competitive modulation device. However, it should be noticed that all MIM plasmonic modulators possess a relatively large IL due to the ohmic loss brought by metal, and GST-embedded MIM modulators will possess a little more IL since GST also brings intrinsic loss.

4 Conclusion

In summary, we investigate three structures to show that GST can be efficiently utilized to construct the high-performance modulator and switch in the plasmonic MIM system. Besides, this work focuses on telecommunication band, aiming to provide more solutions for on-chip photonic systems for information processing. Furthermore, the small footprint and easy fabrication of the proposed structures can have advantages in applications on more future compact all-optical circuits.

Acknowledgments

References

1. D. K. Gramotnev and S. I. Bozhevolnyi, "Plasmonics beyond the diffraction limit," *Nat. Photonics* **4**(2), 83–91 (2010).
2. E. A. Marcatili, "Dielectric rectangular waveguide and directional coupler for integrated optics," *Bell Syst. Tech. J.* **48**(7), 2071–2102 (1969).

3. D. Deslandes and K. Wu, "Integrated microstrip and rectangular waveguide in planar form," *IEEE Microwave Wireless Compon. Lett.* **11**(2), 68–70 (2001).

4. S. I. Bozhevolnyi et al., "Channel plasmon subwavelength waveguide components including interferometers and ring resonators," *Nature* **440**(7083), 508–511 (2006).

5. Y. Fang and M. Sun, "Nanoplasmonic waveguides: towards applications in integrated nanophotonic circuits," *Light Sci. Appl.* **4**(6), e294 (2015).

6. J. A. Dionne et al., "Plasmon slot waveguides: towards chip-scale propagation with sub-wavelength-scale localization," *Phys. Rev. B* **73**(3), 035407 (2006).

7. P. Neutens et al., "Electrical detection of confined gap plasmons in metal-insulator-metal waveguides," *Nat. Photonics* **3**(5), 283–286 (2009).

8. H. Lu, G. Wang, and X. Liu, "Manipulation of light in MIM plasmonic waveguide systems," *Chin. Sci. Bull.* **58**(30), 3607–3616 (2013).

9. A. Kriesch et al., "Functional plasmonic nanocircuits with low insertion and propagation losses," *Nano Lett.* **13**(9), 4539–4545 (2013).

10. H. Lu et al., "Tunable band-pass plasmonic waveguide filters with nanodisk resonators," *Opt. Express* **18**(17), 17922–17927 (2010).

11. Z. Zhang et al., "Plasmonic filter and demultiplexer based on square ring resonator," *Appl. Sci.* **8**(3), 462 (2018).

12. G. Wang et al., "Tunable multi-channel wavelength demultiplexer based on MIM plasmonic nanodisk resonators at telecommunication regime," *Opt. Express* **19**(4), 3513–3518 (2011).

13. K. Nakayama et al., "Passive plasmonic demultiplexers using multimode interference," *J. Lightwave Technol.* **36**(10), 1979–1984 (2018).

14. Y. Binfeng et al., "Design of a compact and high sensitive refractive index sensor base on metal–insulator–metal plasmonic Bragg grating," *Opt. Express* **22**(23), 28662–28670 (2014).

15. L. Chen et al., "Numerical analysis of a near-infrared plasmonic refractive index sensor with high figure of merit based on a fillet cavity," *Opt. Express* **24**(9), 9975–9983 (2016).

16. G. Wang, H. Lu, and X. Liu, "Trapping of surface plasmon waves in graded grating waveguide system," *Appl. Phys. Lett.* **101**(1), 013111 (2012).

17. Z. Zhang et al., "Plasmon-induced transparency based on aperture-coupled cascade resonators without gap," *Superlattices Microstruct.* **123**, 138–143 (2018).

18. Z. Zhang et al., "All-optical multi-channel switching at telecommunication wavelengths based on tunable plasmon-induced transparency," *Opt. Commun.* **425**, 196–203 (2018).

19. X. Yang et al., "Ultracompact all-optical logic gates based on nonlinear plasmonic nanocavities," *Nanophotonics* **6**(1), 365–376 (2017).

20. Z. Chai et al., "Chip-integrated all-optical diode based on nonlinear plasmonic nanocavities covered with multicomponent nanocomposite," *Nanophotonics* **6**(1), 329–339 (2017).

21. M. T. Hill et al., "Lasing in metal–insulator–metal sub-wavelength plasmonic waveguides," *Opt. Express* **17**(13), 11107–11112 (2009).

22. Z. Yu et al., "Gain-induced switching in metal-dielectric-metal plasmonic waveguides," *Appl. Phys. Lett.* **92**(4), 041117 (2008).

23. Z. Zhang et al., "Active enhancement of slow light based on plasmon-induced transparency with gain materials," *Materials* **11**(6), 941 (2018).

24. H. Lu et al., "Graphene-supported manipulation of surface plasmon polaritons in metallic nanowaveguides," *Photonics Res.* **5**(3), 162–167 (2017).

25. Z. Chen et al., "Surface plasmon characteristics based on graphene-cavity-coupled waveguide system," *Solid State Commun.* **280**, 50–55 (2018).

26. C. Song et al., "Wavelength-sensitive PIT-like double-layer graphene-based metal–dielectric–metal waveguide," *Appl. Opt.* **57**(33), 9770–9776 (2018).

27. Y. Li and C. Argyropoulos, "Tunable nonlinear coherent perfect absorption with epsilon-near-zero plasmonic waveguides," *Opt. Lett.* **43**(8), 1806–1809 (2018).

28. Y. Huang, C. Min, and G. Veronis, "Broadband near total light absorption in non-PT-symmetric waveguide-cavity systems," *Opt. Express* **24**(19), 22219–22231 (2016).

29. M. Wuttig, H. Bhaskaran, and T. Taubner, "Phase-change materials for non-volatile photonic applications," *Nat. Photonics* **11**(8), 465–476 (2017).

30. N. Youngblood et al., "Tunable volatility of $Ge_2Sb_2Te_5$ in integrated photonics," *Adv. Funct. Mater.* **29**(11), 1807571 (2019).

31. M. H. Lankhorst, B. W. Ketelaars, and R. A. Wolters, "Low-cost and nanoscale non-volatile memory concept for future silicon chips," *Nat. Mater.* **4**(4), 347–352 (2005).

32. C. Ríos et al., "Integrated all-photonic non-volatile multi-level memory," *Nat. Photonics* **9**(11), 725–732 (2015).

33. J. Feldmann et al., "All-optical spiking neurosynaptic networks with self-learning capabilities," *Nature* **569**(7755), 208–214 (2019).

34. M. Rudé et al., "Optical switching at 1.55 μm in silicon racetrack resonators using phase change materials," *Appl. Phys. Lett.* **103**(14), 141119 (2013).

35. J. Zheng et al., "GST-on-silicon hybrid nanophotonic integrated circuits: a non-volatile quasi-continuously reprogrammable platform," *Opt. Mater. Express* **8**(6), 1551–1561 (2018).

36. C. Rios et al., "Controlled switching of phase-change materials by evanescent-field coupling in integrated photonics," *Opt. Mater. Express* **8**(9), 2455–2470 (2018).

37. Q. Wang et al., "Optically reconfigurable metasurfaces and photonic devices based on phase change materials," *Nat. Photonics* **10**(1), 60–65 (2016).

38. B. Gholipour et al., "An all-optical, non-volatile, bidirectional, phase-change meta-switch," *Adv. Mater.* **25**(22), 3050–3054 (2013).

39. Y. G. Chen et al., "Hybrid phase-change plasmonic crystals for active tuning of lattice resonances," *Opt. Express* **21**(11), 13691–13698 (2013).

40. E. D. Palik, *Handbook of Optical Constants of Solids*, Vol. **3**, Academic Press, Cambridge, Massachusetts (1998).

41. C. H. Chu et al., "Active dielectric metasurface based on phase-change medium," *Laser Photonics Rev.* **10**(6), 986–994 (2016).

42. J. Tian et al., "Active control of anapole states by structuring the phase-change alloy $Ge_2Sb_2Te_5$," *Nat. Commun.* **10**(1), 396 (2019).

43. Z. He et al., "Theoretical analysis of ultrahigh figure of merit sensing in plasmonic waveguides with a multimode stub," *Opt. Lett.* **41**(22), 5206–5209 (2016).

44. M. A. Bavil, L. Gao, and X. Sun, "A compact nanoplasmonics filter and intersection structure based on utilizing a slot cavity and a Fabry–Perot resonator," *Plasmonics* **8**(2), 631–636 (2013).

45. X. S. Lin and X. G. Huang, "Tooth-shaped plasmonic waveguide filters with nanometeric sizes," *Opt. Lett.* **33**(23), 2874–2876 (2008).

46. T. Wang et al., "Analogue of electromagnetically induced transparency in integrated plasmonics with radiative and subradiant resonators," *Opt. Express* **22**(18), 21529–21534 (2014).

47. W. Cai, J. S. White, and M. L. Brongersma, "Compact, high-speed and power-efficient electrooptic plasmonic modulators," *Nano Lett.* **9**(12), 4403–4411 (2009).

48. C. Min and G. Veronis, "Absorption switches in metal–dielectric–metal plasmonic waveguides," *Opt. Express* **17**(13), 10757–10766 (2009).

49. Z. J. Zhong et al., "Sharp and asymmetric transmission response in metal–dielectric–metal plasmonic waveguides containing Kerr nonlinear media," *Opt. Express* **18**(1), 79–86 (2010).

50. X. Piao, S. Yu, and N. Park, "Control of Fano asymmetry in plasmon induced transparency and its application to plasmonic waveguide modulator," *Opt. Express* **20**(17), 18994–18999 (2012).

51. A. Haddadpour et al., "Highly compact magneto-optical switches for metal–dielectric–metal plasmonic waveguides," *Opt. Lett.* **41**(18), 4340–4343 (2016).

52. V. V. Temnov et al., "Active magneto-plasmonics in hybrid metal-ferromagnet structures," *Nat. Photonics* **4**(2), 107–111 (2010).

53. Q. F. Zhang et al., "Ultrafast optical Kerr effect of Ag–BaO composite thin films," *Appl. Phys. Lett.* **82**(6), 958–960 (2003).

54. D. Loke et al., "Breaking the speed limits of phase-change memory," *Science* **336**(6088), 1566–1569 (2012).

55. M. Pu et al., "Directional coupler and nonlinear Mach–Zehnder interferometer based on metal–insulator–metal plasmonic waveguide," *Opt. Express* **18**(20), 21030–21037 (2010).

56. T. Cao et al., "Broadband polarization-independent perfect absorber using a phase-change metamaterial at visible frequencies," *Sci. Rep.* **4**, 3955 (2014).

57. Z. Zhang et al., "Chipscale plasmonic modulators and switches based on metal–insulator–metal waveguides with $Ge_2Sb_2Te_5$," arXiv:1907.00767 (2019).

Biographies of the authors are not available.